PCCP

Accepted Manuscript




ROYAL SOCIETY OF CHEMISTRY

www.rsc.org/pccp

Cite this: DOI: 10.1039/c0xx00000x

www.rsc.org/xxxxxx

ARTICLE TYPE

# Electronic and transport properties of $LiCoO_2$

**Bohdan Andriyevsky,*[a,b] Klaus Doll[b] and Timo Jacob[b,c]**

***Received (in XXX, XXX) Xth XXXXXXXXX 20XX, Accepted Xth XXXXXXXXX 20XX***
**DOI: 10.1039/b000000x**

Using first principles density functional theory (DFT), the electronic and magnetic properties as well as the Li-ion migration in $LiCoO_2$ have been studied with a gradient corrected functional. The magnetic properties were in addition also investigated with a gradient corrected functional in combination with an on-site repulsion $U$, and a hybrid functional. We find $LiCoO_2$ to be non-magnetic at ambient conditions. A magnetic ground state can be obtained by a volume expansion corresponding to a negative pressure of −8 GPa due to a competition of Hund's rules favoring magnetism on the $Co^{3+}$ ions and the crystal field splitting, which suppresses magnetism at zero pressure. The barrier for lithium transport is determined to be 0.44 eV from nudged elastic band (NEB) calculations on the system $Li_{0.917}CoO_2$.

[a] *Faculty of Electronics and Computer Sciences, Koszalin University of Technology, Śniadeckich Str. 2, PL-75-453, Koszalin, Poland. Fax: +48943433479; Tel: +48943478690; E-mail: bohdan.andriyevskyy@tu.koszalin.pl*
[b] *Institute of Electrochemistry, Ulm University, Albert-Einstein-Allee 47, D-89069 Ulm, Germany. klaus.doll@uni-ulm.de*
[c] *Helmholtz Institute Ulm (HIU), Albert-Einstein-Allee 11, D-89081 Ulm, Germany. E-mail: timo.jacob@uni-ulm.de*

## Introduction

Lithium cobalt oxide $LiCoO_2$ is used in rechargeable lithium ion batteries. Presently, lithium ion batteries are mainly based on $LiCoO_2$ as cathode, a lithium ion conducting organic polymer as the electrolyte, and graphite as the anode [1, 2]. Due to the layered crystal structure of $LiCoO_2$, which has rhombohedral symmetry and belongs to the space group $R\bar{3}m$, this material is ideally suited to accommodate lithium in concentrations, which may change over a relatively large range [3]. This has led to wide applications of $LiCoO_2$ with deintercalated lithium $Li_xCoO_2$ ($x < 1$) as cathode material in solid-state batteries.

Numerous phenomena should be taken into account to obtain mathematical models for a solid-state battery [4, 5]. One of the crucial points of these models is the low activation energy for electric transport of solid electrodes and electrolytes. This activation energy is generally dependent on the electronic structure of the material, which can be changed by modifying the chemical elements contained, and external influences. It was shown experimentally [6] that the grain interior is decisive for ion conduction properties such as barriers, and not the grain boundary. The electronic band structure of $LiCoO_2$ has been previously studied using first principles methods [7 - 16]. The top valence and bottom conduction bands are formed mainly by the hybridized *d*-states of cobalt and *p*-states of oxygen. Band structure and total energy calculations were also performed on layered $LiCoO_2$ (rhombohedral, space group $R\bar{3}m$) and $Li_{0.5}CoO_2$ (monoclinic, space group $P2/m$) by the periodic Hartree−Fock method, which overestimates the band gap compared to DFT-based calculations [7, 14, 16] . The experimental band gap $E_g$ is about 1.7 – 2.7 eV [16 - 21].

Due to the presence of cobalt atoms, magnetic properties are also an interesting target to be studied. Magnetic susceptibility measurements [21, 22], X-ray photoelectron spectroscopic analysis [23] and band structure calculations [7] confirmed that the $Co^{3+}$ ions are in a low-spin state ($t_{2g}^6$) with $S = 0$ at ambient temperature. Nevertheless, the $\mu^+$-SR experiments on $LiCoO_2$ [24 – 26] have indicated the possible formation of static antiferromagnetic (AF) order below 30 K ($=T_N$), although the volume fraction of the AF ordered phase is estimated as only ~10%. It was suggested that the observed magnetism is not induced by impurities but is an intrinsic behavior. It is thought that a cobalt charge fluctuation $2Co^{3+} \rightarrow Co^{2+} + Co^{4+}$ occurs at low temperature, corresponding to the electron configurations $2t_{2g}^6 \rightarrow t_{2g}^6 e_g^1 + t_{2g}^5$ [27].

In the present study we have calculated the electronic band structure and related properties of $LiCoO_2$ for the relaxed crystal structure and for the compressed and expanded crystal unit cells. In the course of these calculations, one of the aims was to study the magnetic ordering in $LiCoO_2$ caused by the changes of the unit cell volume and Hubbard $U$-parameter [28, 29] of the cobalt atom. Concerning possible magnetic solutions, we focused on the ferromagnetic case where all cobalt spins are aligned parallel. Another point of the investigation was the activation energy for Li-ion migration in $LiCoO_2$, which was studied using the NEB method. The dielectric permittivity $\varepsilon_\infty$ (electronic polarizability) was also investigated. These results can be used to study the correlation between the properties of Li-ion diffusion in a host crystalline matrix and the corresponding change of the electronic polarizability. Such a correlation may take place due to the local polarization of the host crystalline matrix caused by Li-ions moving in the diffusion process. The importance of the electronic polarizability for the analysis of structural features of Li-containing garnets is discussed in Ref. [30].

## Computational details

Electronic structure calculations were mainly performed using the CASTEP code (CAmbridge Serial Total Energy Package) [31] based on density functional theory (DFT) and a plane-wave basis set. The generalized gradient approximation with the Perdew−Burke−Ernzerhof functional (GGA-PBE) for the exchange and correlation effects [32] together with ultrasoft pseudopotentials [33] was used for the calculations. In addition, the influence of a Hubbard parameter $U$ on the Co site was explored. A cutoff energy of 340 eV was assumed in the plane-wave basis set. During the self-consistent electronic minimization, the eigen-energy convergence tolerance was chosen to be $2.4\cdot10^{-7}$ eV and the tolerance for the electronic total energy convergence during optimization was $1.0\cdot10^{-5}$ eV. The corresponding maximum ionic force tolerance was $3\cdot10^{-2}$ eV/Å and the maximum stress component tolerance was $5\cdot10^{-2}$ GPa. The optimization (relaxation) of the atomic positions and crystal unit cell parameters was performed at various values of the external hydrostatic pressure. Subsequently, the electronic properties, such as the total energy $E$, band dispersion $E(k)$, density of states (DOS), and dielectric permittivity $\varepsilon_\infty$ were computed at the respective optimized geometry. 110 $k$-points in the irreducible Brillouin zone were used, as well as a smearing of 0.1 eV.

In the present investigation, the first-principles code CRYSTAL [34] was also used, which employs a local basis set. A full geometry optimization [35] was performed and the $E(V)$ curves were computed for various configurations. The calculations were done within the framework of the hybrid functional B3LYP for the exchange and correlation part of the Hamiltonian. The following basis sets for the constituent atoms of $LiCoO_2$ were used: [2$s$1$p$] for Li (1$s$ as in [36], and one $sp$ shell with exponent 0.514), [5$s$4$p$2$d$] for Co (as in [37] but with outermost $sp$ exponents 1.4946, 0.5985 and $d$ 0.2824 instead of 1.4914, 0.6031 and 0.3011) and [4$s$3$p$] for O (as in [38], outermost $sp$ exponents 0.4764 and 0.1802). A $\boldsymbol{k}$-point sampling net of the size 8×8×8 was used. No smearing was applied.

VASP (Vienna *ab-initio* Simulation Package) [39] was used to calculate the activation energies $E_a$ for Li-ion migration in $LiCoO_2$ (using NEB) as well as the electronic dielectric permittivity $\varepsilon_\infty$. Here the projector-augmented wave method with the GGA-PBE exchange and correlation functionals were used. A cutoff energy $E_{cutoff}$ of 520 eV for the plane waves, 10 irreducible $\boldsymbol{k}$-points and a smearing of 0.2 eV were used for the calculations on the crystal supercell of the size 2×2×1 (the volume of the supercell corresponds to $V_{sc}$ = 394.4 Å$^3$).

With this choice of codes, the following properties were computed: the band structure, in order to compare with the experiment, e.g. the value of the gap. Also, the influence of hybrid functional and an additional on-site repulsion $U$ can be seen in the band structure. Technically, it is interesting to compare two codes with different approaches (plane-wave pseudopotential versus localized Gaussian basis set), in order to assure the correctness of both approaches. This is done for the band structure, when the same functional is used with both codes. The magnetic ground state of the present system is not immediately obvious. A method for studying this more detailed is to employ a hybrid functional which favors magnetic solutions more than a standard functional. This can be efficiently done with the CRYSTAL code. On the other hand, it is also possible to study the switch to magnetic solutions as a function of $U$. This allows to estimate the order of magnitude when magnetic solutions can be expected. This is implemented in CASTEP and was performed with this code. Finally, the nudged elastic band method is efficiently implemented in VASP, and thus can be used to study lithium ion transport. As a side issue, the optical properties such as the dielectric permittivity were studied. As a whole, ground state properties and transport properties are computed.

## Results and discussion

The features of the non-spin-polarized band structures (Fig. 1) are in good agreement with the literature [8, 13, 16]. The band gap $E_g$ at the GGA-PBE level is 1.02 eV (see Fig. 1a), and at the B3LYP level 4.13 eV (Fig. 1b). This is similar to transition metal oxides such as NiO or CoO, where the gap is below 1 eV with PBE, but around 4 eV with B3LYP [40]. The underestimation of the band gap with standard functionals such as PBE can be explained due to the artificial self-interaction, which is not accounted for. The B3LYP result still shows some deviation from the experimental band gap $E_g$ of $LiCoO_2$, where the literature values are in the range of $E_g$ = 1.7−2.7 eV [16 - 21]. Further improvements might be possible with many body techniques such as Hedin's $GW$ approach or the Bethe-Salpeter equation [41, 42]. The present results are in good agreement with the previous studies based on the same functionals [16]. At the relaxed crystal structure of $LiCoO_2$, the optical band gap $E_g$ is found to be indirect along the LZ-direction in the Brillouin zone (Fig. 1). The band structures obtained with two different program codes (CRYSTAL09 and CASTEP) using the same xc-functional (here PBE) are very similar. This is a confirmation that the results from two different approaches (plane-wave pseudopotential versus localized Gaussian basis set) compare well. The three top valence bands and the two bottom conduction bands of $LiCoO_2$, being mainly of $d$-character, are characterized by a relatively small dispersion $E(\boldsymbol{k})$, whereas the six deeper valence bands, being mainly of oxygen $p$-character, show a larger dispersion.

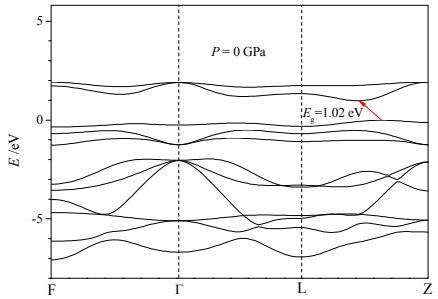


a)

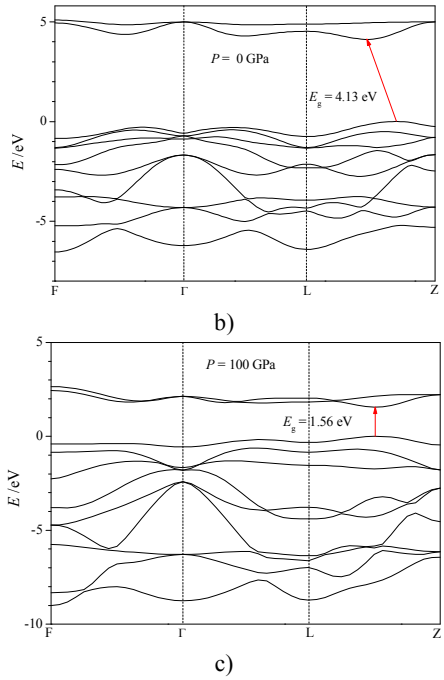


**Figure 1.** Band structures of $LiCoO_2$ in the primitive unit cell containing four atoms, at the level of PBE (a) and B3LYP (b) with CRYSTAL09 (a and b) and with PBE and the CASTEP (c) code. The calculations are non-spin-polarized. Figs. 1a and b correspond to the relaxed structure at 0 GPa and Fig. 1c to the compressed structure at 100 GPa.

The electronic structure and related properties were also studied as a function of the unit cell compression (expansion) caused by hydrostatic pressure. The band gap $E_g$ changes from an indirect to a direct gap under pressure (Fig. 1c). The valence band width increases, and the total width of the top nine valence bands increases from 7 to 9 eV when going from 0 to 100 GPa (Fig. 1a, 1c). The optical band gap is between the occupied and empty Co *d*-states and is an increasing nonlinear function of the pressure *P* below 100 GPa (Fig. 2a). Applying an external pressure reduces the Co−O distances and increases the crystal field splitting that leads to an increasing gap. The band gap $E_g$ was fitted as a function of an inverse average unit cell dimension

$$d^{-1} = V^{-1/3}, \quad (1)$$

where *V* is the unit cell volume of the primitive cell. $E_g$ can be remarkably well fitted with a linear dependency $E_g = a + bd^{-1}$ with the coefficients $a = -3.86$ eV and $b = 17.64$ eV·Å (Fig. 2b).

The electronic density of states is displayed in Fig. 3a. The top valence bands in the range from −1.5 to 0 eV are mainly formed by cobalt *d*-states, whereas the hybridization of oxygen *p*- and cobalt *d*-states is larger in the range up to 2.5 eV of the conduction bands (Fig. 3a). The partial density of states shows that the *p*-bands are shifted to lower energies with respect to the top of the valence bands, when pressure is applied. On the other hand, due to the reduced distances and thus larger crystal field splitting, the unoccupied *d*-bands are shifted upwards with respect to the top of the valence bands, and thus the band gap increases (Fig. 3a).

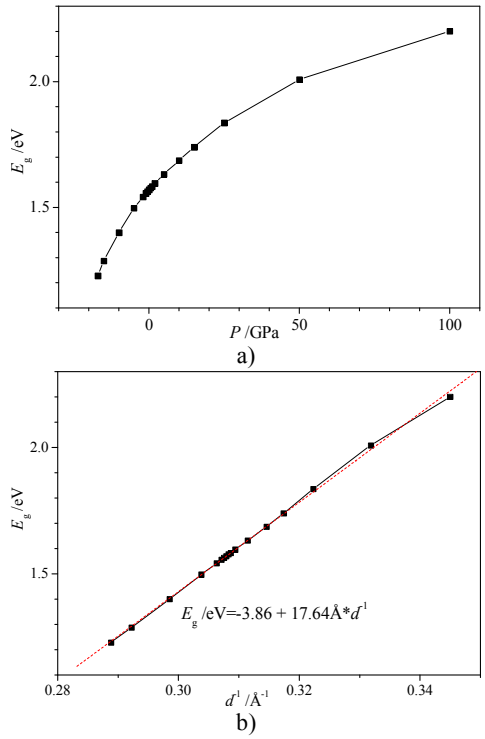


**Figure 2.** Dependencies of the optical band gap $E_g$ upon the external pressure *P* and upon the inverse average unit cell dimension $d^{-1}$ (b) of $LiCoO_2$ with the PBE-GGA exchange and correlation functional (non spin polarized).

To study magnetic properties, the electronic structure of $LiCoO_2$ was calculated spin polarized and in the framework of the DFT+*U* approach. Here, the on-site repulsion on the Co atom is varied by applying a Hubbard *U*. Large *U* values lead to magnetic solutions as this favors single-occupancy of the *d*-orbitals. For a value of $U_{Co} = 2.5$ eV, the solution remains non-magnetic (Fig. 3b). For *U* around 5 eV, however, the characteristic asymmetry of DOS indicates the non-zero total spin (Fig. 3c). Here the occupied Co *d*-states are pushed below the O *p*-states, which indicates that such a *U* value is rather large.

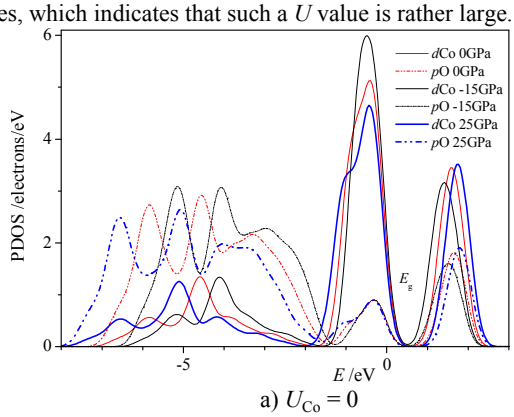

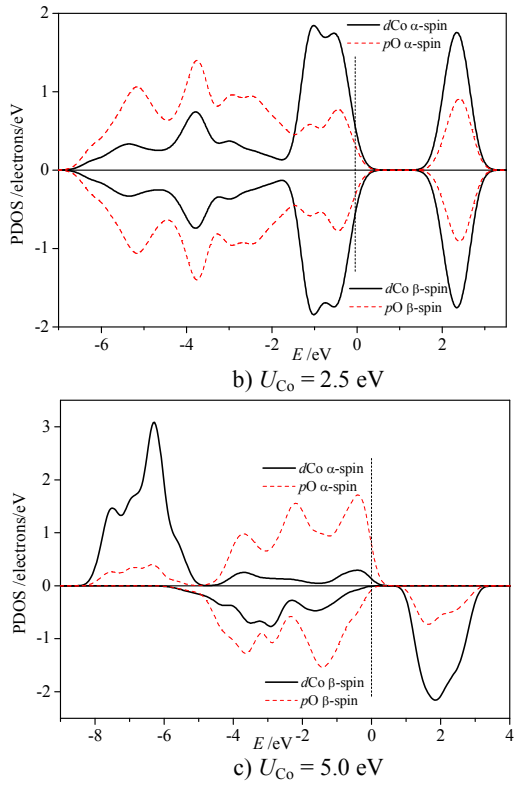


**Figure 3.** (a) Partial density of states of $LiCoO_2$ at external pressures -15 GPa, 0 GPa, 25 GPa, from non-spin-polarized calculations. The PBE functional was used; (b, c) Partial densities of states of $LiCoO_2$ with the PBE functional and an additional Hubbard parameter $U_{Co}$ of 2.5 eV (b) and 5 eV (c). The latter calculations were spin-polarized, without external pressure, *i.e.* at 0 GPa.

The dependency of the total energy $E$ upon the volume of primitive unit cell $V$ is shown in Fig. 4a using the GGA(PBE)+$U$ formalism with different magnitudes of the $U$ parameter for Co. The equilibrium unit cell volume $V_e$, corresponding to the minimum in the $E(V)$ curve, is found to be almost independent on the $U$-parameter in the range between 0 and 2.5 eV, where the total spin moment of the crystal was equal to zero (Fig. 4a). For larger $U$ values, magnetic solutions become energetically favorable. Correspondingly, the equilibrium unit cell volume $V_e$ for the value $U$ = 5 eV is larger (Fig. 4a). These results are to be expected, as a larger $U$ value enhances the importance of obeying Hund's rules for the $Co^{3+}$ ion, and thus favors a magnetic ground state. A strong crystal electric field would however suppress magnetism. This leads to a larger equilibrium volume for the magnetic solution, which reduces the crystal field splitting. There is thus a competition of electron−electron interaction (characterized by $U$) and the local environment (crystal field effects). A larger Coulomb repulsion $U$ leads to magnetic solutions being more favorable. Similarly, enlarging the volume reduces the crystal field splitting and thus also favors magnetism.

A related approach is therefore to enlarge the volume, and search for a possible transition to a magnetic ground state. This was done with the B3LYP exchange−correlation functional (see Fig. 4b). First, in the non-magnetic case, the equilibrium volume $V_e$ and bulk modulus $B$ are rather close for B3LYP and GGA-PBE and are 99.26 Å$^3$ and 102.69 Å$^3$ (for the crystallographic unit cell) and $B$ = 50.0 GPa and 46.2 GPa. The optimized crystallographic unit cell dimensions correspond to $a$ = 2.846 Å, $c$ = 14.15 Å (B3LYP) and $a$ = 2.888 Å, $c$ = 14.22 Å (GGA-PBE). This is also close to the experimental value of the equilibrium volume $V_e^{(exp)}$ = 97 Å$^3$ ($a$ = 2.82 Å, $c$ = 14.1 Å) [43]. When enlarging the volume, however, the magnetic solution becomes favorable. This is due to the enlarged Co−O distances and thus reduction of the crystal field splitting at enlarged volume. The corresponding enthalpies are displayed in Fig. 5, and the magnetic state becomes favorable at a negative pressure of about −8 GPa, corresponding to a volume expansion.

The projected densities of states at the equilibrium volume of 33.1 Å$^3$ and at a volume of 52.1 Å$^3$ of the primitive unit cell are displayed in Fig. 6. The contributions from Co $d$ and O $p$ are dominant, and the other contributions are thus not displayed. The DOS of the non-magnetic solution at equilibrium volume, and the spin-polarized DOS at expanded volume are qualitatively similar to the results from GGA+$U$ in Figs. 3(b) and (c), respectively.

Stoichiometric $LiCoO_2$ is found to have $Co^{3+}$ atoms in a low spin state ($S$ = 0) and is therefore non-magnetic [23]. Recently, spin/charge fluctuations of Co atoms ($Co^{2+}$, $Co^{3+}$, or $Co^{4+}$) were suggested to lead to magnetism even in the stoichiometric $LiCoO_2$ [25]. A slight displacement of the oxygen ions was proposed as an explanation, leading to a different crystal field and thus changing the magnetic state. Therefore, it is interesting to study possible magnetic solutions as a function of pressure. In addition, the on-site repulsion on the Co atom can be varied by applying a Hubbard $U$. For large $U$, this is expected to lead to magnetic solutions, as this favors single-occupancy of the $d$-orbitals.

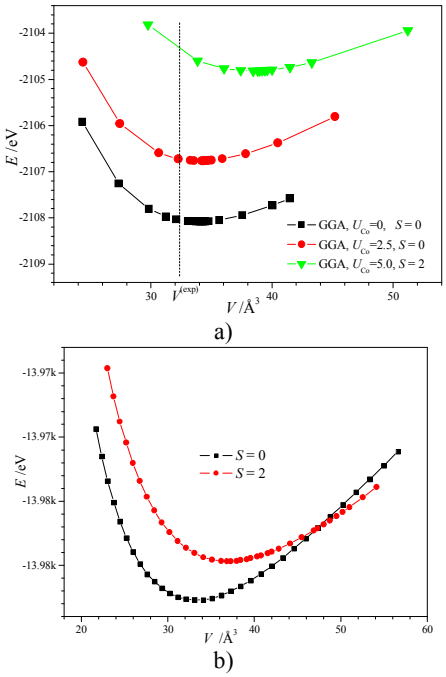


**Figure 4.** Dependencies of total energy $E$ upon the volume of the primitive unit cell $V$ for $LiCoO_2$: (a) with Hubbard $U$-parameter used in GGA+$U$ functional; (b) with the B3LYP functional.

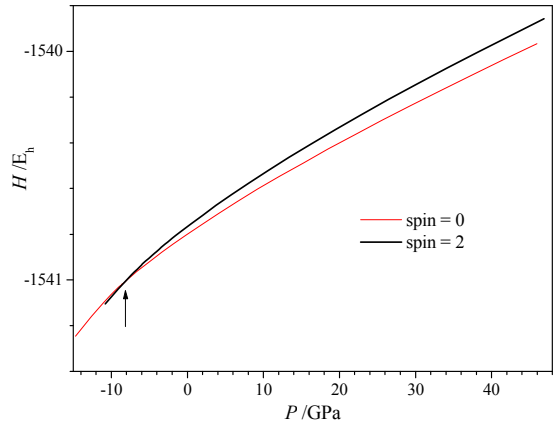


**Figure 5.** Dependencies of enthalpy $H$ upon hydrostatic pressure $P$ of $LiCoO_2$ obtained for non-spin-polarized (thin line) and spin polarized (thick line) conditions, with the B3LYP functional.

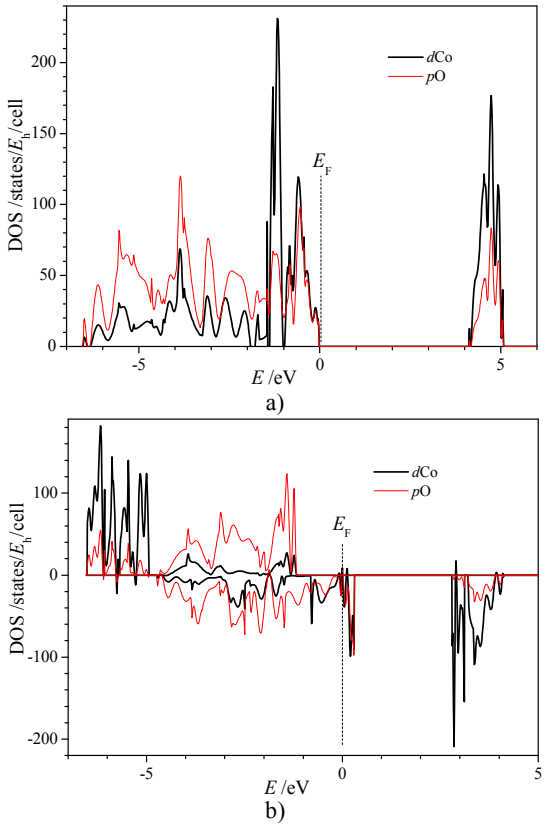


**Figure 6.** Projected density of states of $LiCoO_2$, on the level of B3LYP, at (a) the equilibrium volume of the primitive cell of 33.1 Å$^3$, non-spin-polarized and (b) at an expanded volume of 52.1 Å$^3$, spin-polarized.

To gain a further understanding of the influence of the $U$-parameter for Co on the magnetic ground state, $U$ has been varied in the range from 2.5 eV to 7.0 eV (the default value suggested is 2.5 eV [31]). For each $U$ value, the geometry was fully optimized. The ground state is found to switch from the non-magnetic one to the magnetic with a spin of 4 ħ/2 for $U$ of about ≥ 4.6 eV. The band gap initially increases with $U$ in the range up to $U$ ~ 4.6 eV, which is expected as a result of taking the Coulomb repulsion between localized $d$-electrons into account [28, 29]. When the transition to the magnetic ground state takes place, then the gap is strongly reduced to about 2 eV, due to the different electronic structure: the Co 3$d$ states are pushed below the O $p$-states due to the large $U$ value. For even larger $U$, the gap increases again (Fig. 7). At the transition, the ground state of the $Co^{3+}$ ions changes from the low spin, $S = 0$, to the high spin state, $S = 2$. The ionicity of cobalt and oxygen slightly increases, from -0.8 |e| to -0.9 |e| (oxygen), and from +0.6 |e| to +0.8 |e| (cobalt). This is probably due to the increased volume in the magnetic state. The lithium charge is essentially constant around +0.96 |e|.

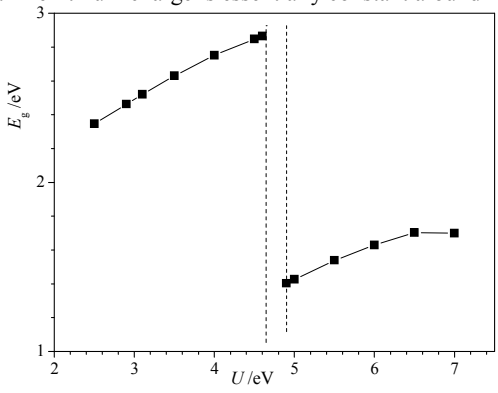


**Figure 7.** Dependency of the band gap $E_g$ on the Hubbard $U$ parameter for Co, obtained with GGA+$U$, for $LiCoO_2$.

$LiCoO_2$ based materials are widely used in solid state batteries, and therefore transport properties are important. Diffusion coefficients have been measured experimentally (for an overview see e.g. [44, 45]). For this purpose, methods such as the potentiostatic intermittent titration technique (PITT), electrochemical impedance spectroscopy (EIS), potential step chronoamperometry (PSCA), or electrochemical voltage spectroscopy (EVS) have been employed. The measured values from PITT are in the range (all in cm$^2$/s) of $10^{-12}$ to $10^{-11}$ (PITT, EIS) [46], $10^{-12}$ [47], $10^{-12}$ to $10^{-10}$ [48], $10^{-12}$ to $10^{-10}$ (PITT, EIS) [49], $10^{-12}$ to $10^{-11}$ (PITT, EIS) [50], $10^{-12}$ to $10^{-11}$ (PITT, EIS) [51], $10^{-11}$ to $10^{-10}$ [52]. Further values from EIS are in the range $10^{-10}$ to $10^{-9}$ [53]. Larger values have also been obtained, such a $10^{-10}$ to $10^{-7}$ [54] (PSCA, EIS), $10^{-9}$ (EVS) [55], $10^{-9}$ to $10^{-8}$ (PITT) [56]. In addition, from nuclear magnetic resonance (NMR) experiments, a barrier of 0.08 - 0.3 eV was deduced, depending on the stoichiometry and thus structural parameters [57].

The diffusion coefficients have been measured as a function of voltages, and the voltages can subsequently be mapped on Li concentrations in $Li_xCoO_2$, see e.g. [46-48, 50-52, 55, 58, 59]. Thus, the diffusion coefficient $D$ can be related to the Li concentration. This can be connected with an activation energy $E_a$ via the estimate $D = a^2 \cdot \nu \cdot \exp[-E_a/(k_B T)]$, where ν is the attempt frequency, typically of the order $10^{13}$ s$^{-1}$, and $a$ the hopping distance. With e.g. $D = 10^{-11}$ cm$^2$/s, $a$ of around 3 Å, and $\nu = 10^{13}$ s$^{-1}$, at $T = 300$ K an activation energy of about 0.5 eV would be obtained.

These data are in good agreement with barriers computed with the nudged elastic band method [6, 60],or the synchronous transit method [47]. Possible factors which have an impact were also explored computationally in [61]. Earlier calculations based on molecular dynamics with an empirical force field also resulted in

a barrier of the order of 0.3 eV [62]. However, it was noted that even large simulation boxes with over 1000 atoms and times of 5 to 15 ps were too short (at ambient temperature) to observe hopping of lithium ions from one site to another. For the system $LiFePO_4$, long runs of the order of hundreds of picoseconds were required to obtain reliable results for mean square displacements as a function of time [63], whereas ab initio molecular dynamics for the same system remains challenging due to the simulation time, even at elevated temperatures of 2000 K, as was shown in [64].

In order to investigate the lithium ion transport, the energetics of the migration of the ions has been computed with the nudged elastic band method as implemented in the VASP code [39]. A supercell containing 2×2×1 units of the crystallographic unit cell of $LiCoO_2$ ($a = b = 5.698$ Å, $c = 14.023$ Å) was generated. This supercell contains 47 atoms and one lithium vacancy ($Li_{0.917}CoO_2$). The NEB-images were obtained by displacing one Li-ion along the *a*-axis in the *xy*-plane towards the vacancy (Fig. 8a). The shape of the unit cell was kept fixed during the NEB calculations. Due to the missing lithium atom, one electron less can be transferred to cobalt. Thus, a magnetic solution carrying an initial spin of 1/2 was explored, corresponding to a possible spin of a $Co^{4+}$ ion in this surrounding. However, during the self-consistent field cycles, the magnetic moment vanished, and the final state was a non-magnetic, metallic state. There is thus no evidence for a spin-polarization in this case, which is consistent with earlier findings [3]. The results presented here thus refer to non-spin-polarized calculations.

The Li-ion migration path from the initial site to the vacancy obtained deviates from the straight line. The path and the computed energy barrier $\Delta E = 0.44$ eV (Fig. 8b) is in good agreement with earlier results reported in Refs. [6, 60].

The Bader electronic charges of the Li ions in the three lithium layers of the supercell have been calculated along the path as a function of the same distance along the *a*-axis (Fig. 8c). At the saddle point, where the total energy is at its maximum along the path, the Bader electronic charge for lithium is about −2.136 |e|, and the total charge thus 0.864 |e| (Fig. 8c). The Bader electronic charge is thus largest in magnitude along the migration path; or in other words lithium is least ionic. At this point, the lithium ions are also very close to the neighboring oxygen ions, which leads to a reduced ionicity. The $CoO_2$ electronic charge will thus be reduced at the saddle point, which decreases its electronic polarizability.

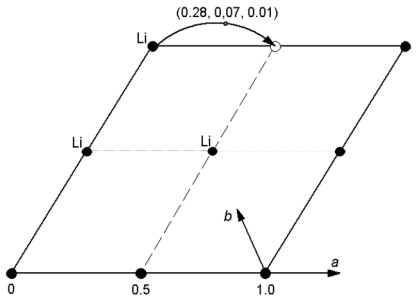


a)

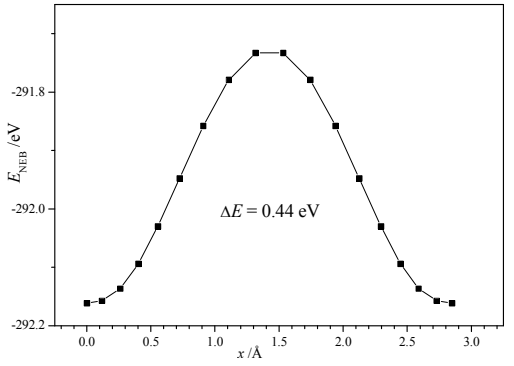


b)

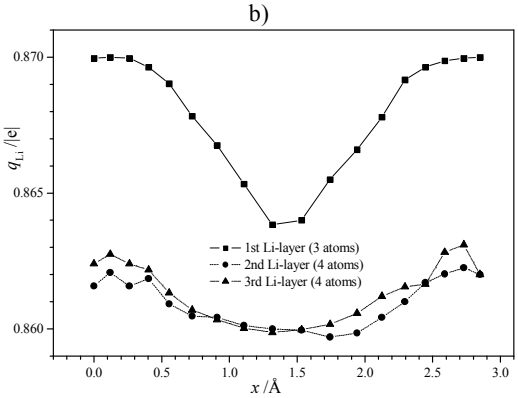


c)

**Figure 8.** Positions of Li-atoms (black circles) and Li-vacancy (white circle) in one *z*-layer of a 2×2×1 supercell of $Li_{0.917}CoO_2$ and path of the migrating Li-ion (a). Dependencies of the total energy *E* obtained with the PBE functional (b) and Bader charge of lithium ions $q_{Li}$ (c) on the position *x* of the migrating Li ions. The values of $x = 0$ and 2.85 Å correspond to the crystallographic positions (0, 0, 0) and (0.5, 0, 0) in the 2×2×1 supercell. The results presented are from non-spin-polarized calculations.

The real part of the dielectric permittivities $\varepsilon_1^{(xx)}$ and $\varepsilon_1^{(yy)}$ and $\varepsilon_1^{(zz)}$ was evaluated as function of the position of the lithium ion in the doped system $Li_{0.917}CoO_2$. It is expected that it mainly depends on the valence and conduction bands originating from $CoO_2$. As is shown in Fig. 9, it slightly decreases along the path of lithium migration. This is consistent with a decrease of the polarizability $\alpha_{\text{unit-cell}}$ according to the Clausius−Mossotti relation [65],

$$\frac{M_{\text{unit-cell}}}{\rho}\frac{(\varepsilon-1)}{(\varepsilon+2)} = \frac{4\pi N_A}{3}\alpha_{\text{unit-cell}}, \qquad (2)$$

i.e. $\alpha_{\text{unit-cell}}$ is proportional to $\left(1-\frac{3}{\varepsilon+2}\right)$. A decreasing $CoO_2$ electronic charge and thus decreasing polarizability $\alpha_{\text{unit cell}}$ will thus result in a decreasing dielectric permittivity ε. The anisotropy, $\varepsilon_x \approx \varepsilon_y > \varepsilon_z$ is very high (Fig. 9). The relative changes of the dielectric permittivity ($\Delta\varepsilon_z/\varepsilon_z = 0.054$) are larger than in the other directions ($\Delta\varepsilon_x/\varepsilon_x = 0.011$, $\Delta\varepsilon_y/\varepsilon_y = 0.007$) (Fig. 9). The dielectric permittivity may thus be a useful property to study the migration of lithium ions.

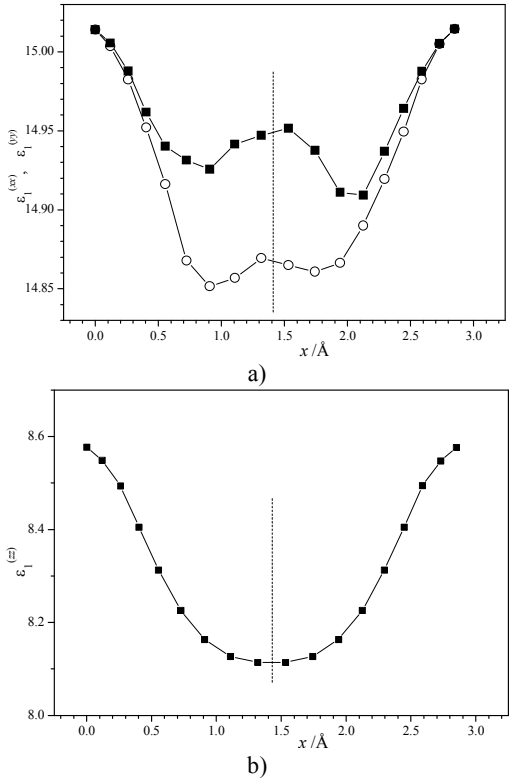


**Figure 9.** Dependencies of the real part of the dielectric permittivity $\varepsilon_1^{(xx)}$ and $\varepsilon_1^{(yy)}$ (a) and $\varepsilon_1^{(zz)}$ (b) of $Li_{0.917}CoO_2$ on the position of the lithium ion. The values of $x$ = 0 and 2.85 Å correspond to the crystallographic positions (0, 0, 0) and (0.5, 0, 0). The results presented are from non-spin polarized calculations.

## Conclusions

The electronic structure of and transport properties within undoped $LiCoO_2$ has been studied by first principles density functional theory. The computed band gap is 1.02 eV using the GGA-PBE exchange−correlation functional, and 4.13 eV with the hybrid functional B3LYP. The ground state is non-magnetic. When applying an external pressure, the band gap increases due to the increasing crystal field splitting. The size of the band gap $E_g$ was found to be proportional to the inverse unit cell dimension $d^{-1} = V^{-1/3}$. A transition from the non-magnetic ($S = 0$) to the magnetic state ($S = 2$) is observed when the unit cell is expanded. This is due to the reduced crystal field splitting, which leads to Hund's rules becoming dominant and thus favoring a magnetic ground state for the $Co^{3+}$ ions. Similarly, with an additional Hubbard $U$ on the Co site, a magnetic ground state becomes preferable for $U$ values larger than ~5 eV.

Transport properties have been studied with the nudged elastic band scheme. A barrier of 0.44 eV was obtained, which is in good agreement with previous simulations. When computing the dielectric permittivity of the crystal along the Li-ion migration path, a decrease is observed around the saddle point. It is thought that this is due to the reduced ionicity and thus also reduced polarizability of $CoO_2$.

## Acknowledgements

The CASTEP calculations were performed in the computer center of Wrocław University of Technology (WCSS) within Accelrys Materials Studio 6.1 package. The VASP calculations were done in the computer center of Warsaw University (ICM) in the framework of the project G26-3. TJ acknowledges support from the European Research Council through the ERC-Starting Grant THEOFUN (Grant Agreement No. 259608). Further, we thank for financial support by the DFG (Deutsche Forschungsgemeinschaft) through the priority program (SPP-1613).

## Notes and references

1. J.R. Owen, *Chem. Soc. Rev.*, 1997, **26**, 259-267.
2. M. Wakihara and O. Yamamoto (Eds.), *Lithium Ion Batteries: Fundamentals and Performance*, WileyVCH, Weinheim, Germany, 1998.
3. A. Van der Ven, M.K. Aydinol, G. Ceder, G. Kresse and J. Hafner, *Phys. Rev. B*, 1998, **58**, 2975-2987.
4. M. Landstorfer and S. Funken, T. Jacob, *Phys. Chem. Chem. Phys.*, 2011, **13**, 12817-12825.
5. M. Landstorfer and T. Jacob, *Chem. Soc. Rev.*, 2013, **42**, 3234-3252.
6. X. Zhu, C. Shen Ong, X. Xu, B. Hu, J. Shang, H. Yang, S. Katlakunta, Y. Liu, X. Chen, L. Pan, J. Ding and R.-W. Li, *Sci. Rep.*, 2013, **3**, 1084.
7. M.T. Czyzyk, R. Potze and G.A. Sawatzky, *Phys. Rev. B*, 1992, **46**, 3729-3736.
8. M.K. Aydinol, A.F. Kohan and G. Ceder, *Phys. Rev. B*, 1997, **56**, 1354-1365.
9. M. Catti, *Phys. Rev. B*, 2000, **61**, 1795-1802.
10. V.R. Galakhov, V.V. Karelina, D.G. Kellerman, V.S. Gorshkov, N.A. Ovechkina and M. Neumann, *Phys. Solid State*, 2002, **44**, 266-273.
11. D. Carlier, A. Van der Ven, C. Delmas and G. Ceder, *Chem. Mater.*, 2003, **15**, 2651-2660.
12. L.Y. Hu, Z.H. Xiong, C.Y. Ouyang, S. Shi, Y. Ji, M. Lei, Z. Wang, H. Li, X. Huang and L. Chen, *Phys. Rev. B*, 2005, **71**, 125433.
13. S. Laubach, S. Laubach, P.C. Schmidt, D. Ensling, S. Schmid, W. Jaegermann, A. Thißen, K. Nikolowski and H. Ehrenberg, *Phys. Chem. Chem. Phys.*, 2009, **11**, 3278-3289.
14. G. Mattioli, M. Risch, A.A. Bonapasta, H. Dau and L. Guidoni, *Phys. Chem. Chem. Phys.*, 2011, **13**, 15437-15441.
15. D. Carlier, J.-H. Cheng, C.-J. Pan, M. Ménétrier, C. Delmas and B.-J. Hwang, *J. Phys. Chem. C*, 2013, **117**, 26493-26500.
16. D. Ensling, A. Thissen, S. Laubach, P.C. Schmidt and W. Jaegermann, *Phys. Rev. B*, 2010, **82**, 195431.
17. P. Ghosh, S. Mahanty, M.W. Raja, R.N. Basu and H.S. Maiti, *J. Mater. Res.*, 2007, **22**, 1162-1167.
18. K. Kushida and K. Kuriyama, *Solid State Commun.*, 2001, **118**, 615-618.
19. J.M. Rosolen and F. Decker, *J. Electroanal. Chem.*, 2001, **501**, 253-259.
20. M.C. Rao and O.M. Hussain, *Eur. Phys. J. Appl. Phys.*, 2009, **48**, 20503-20508.
21. J. van Elp, J.L. Wieland, H. Eskes, P. Kuiper, G.A. Sawatzky, F.M.F. de Groot and T.S. Turner, *Phys. Rev. B*, 1991, **44**, 6090-6103.
22. T.A. Hewston and B.L. Chamberland, *J. Phys. Chem. Solids*, 1987, **48**, 97-108.
23. Tomeno and M. Oguchi, *J. Phys. Soc. Japan*, 1998, **67**, 318-322.
24. J. Sugiyama, H. Nozaki, J.H. Brewer, E.J. Ansaldo, G.D. Morris and C. Delmas, *Phys. Rev. B*, 2005, **72**, 144424.
25. K. Mukai, Y. Ikedo, H. Nozaki, J. Sugiyama, K. Nishiyama, D. Andreica, A. Amato, P.L. Russo, E.J. Ansaldo, J.H. Brewer, K.H. Chow, K. Ariyoshi and T. Ohzuku, *Phys. Rev. Lett.*, 2007, **99**, 087601.

26. J. Sugiyama, Y. Ikedo, H. Nozaki, K. Mukai, D. Andreica, A. Amato, M. Menetrier, D. Carlier and C. Delmas, *Physica B*, 2009, **404**, 769-772.
27. J. Sugiyama, H. Nozaki, J.H. Brewer, E.J. Ansaldo, G.D. Morris and C. Delmas, *Physica B*, 2006, **374–375**, 148-151.
28. A.I. Liechtenstein, V.I. Anisimov and J. Zaanen, *Phys. Rev. B*, 1995, **52**, R5467-R5471.
29. S.L. Dudarev, G.A. Botton, S.Y. Savrasov, C.J. Humphreys and A.P. Sutton, *Phys. Rev. B*, 1998, **57**, 1505-1509.
30. M.P. O'Callaghan and E.J. Cussen, *Solid State Sci.*, 2008, **10**, 390-395.
31. S.J. Clark, M.D. Segall, C.J. Pickard, P.J. Hasnip, M.J. Probert, K. Refson and M.C. Payne, *Zeitschrift für Kristallographie*, 2005, **220**, 567-570.
32. J.P. Perdew, K. Burke and M. Ernzerhof, *Phys. Rev. Lett.*, 1996, **77**, 3865-3868.
33. D. Vanderbilt, *Phys. Rev. B*, 1990, **41**, 7892-7895.
34. R. Dovesi, V.R. Saunders, C. Roetti, R. Orlando, C. M. Zicovich-Wilson, F. Pascale, B. Civalleri, K. Doll, N.M. Harrison, I.J. Bush, Ph. D'Arco and M. Llunell, *User's Manual of CRYSTAL'09* (Torino, Italy, 2009).
35. K. Doll, V. R. Saunders and N. M. Harrison, *Int. J. Quant. Chem.*, 2001, **82**, 1-13; K. Doll, R. Dovesi and R. Orlando, *Theor. Chem. Acc.*, 2004, **112**, 394-402; B. Civalleri, P. D'Arco, R. Orlando, V. R. Saunders and R. Dovesi, *Chem. Phys. Lett.*, 2001, **348**, 131-138.
36. R. Dovesi, C. Roetti, F. Freyria-Fava, M. Prencipe and V. R. Saunders, *Chem. Phys.*, 1991, **156**, 11-19.
37. R. Dovesi, F. Freyria-Fava, C. Roetti and V. R. Saunders, *Faraday Discussion*, 1997, **106**, 173-187.
38. M.D. Towler, N.L. Allan, N.M. Harrison, V.R. Saunders, W.C. Mackrodt and E. Aprà, *Phys. Rev. B*, 1994, **50**, 5041-5056.
39. G. Kresse and D. Joubert, *Phys. Rev.* **59**, 1758 (1999); The guide of VASP https://cms.mpi.univie.ac.at/marsweb/index.php.
40. T. Bredow and A.R. Gerson, *Phys. Rev. B*, 2000, **61**, 5194-5201.
41. F. Fuchs, J. Furthmüller, F. Bechstedt, M. Shishkin and G. Kresse, *Phys. Rev. B*, 2007, **76**, 115109.
42. G. Onida, L. Reining and A. Rubio, *Rev. Mod. Phys.*, 2002, **74**, 601-659.
43. I. Rodrigues, J. Wontcheu and D.D. MacNeil, *Mater. Res. Bull.*, 2011, **46**, 1878-1881.
44. M. Park, X. Zhang, M. Chung, G B. Less and A.M. Sastry, *J. Power Sources*, 2010, **24**, 7904–7929.
45. A. Van Der Ven, J. Bhattacharya and A.A. Belak, *Acc. Chem. Res.*, 2013, **46**, 1216–1225.
46. Y.H. Rho and K. Kanamura, *J. Electrochem. Soc.*, 2004, **151**, A1406-A1411.
47. M. Okubo, Y. Tanaka, H. Zhou, T. Kudo and I. Honma, *J. Phys. Chem. B*, 2009, **113**, 2840–2847.
48. J.M. McGraw, C.S. Bahn, P.A. Parilla, J.D. Perkins, D.W. Readey and D.S. Ginley, *Electrochimica Acta*, 1999, **45**, 187-196.
49. M.D. Levi, G. Salitra, B. Markovsky, H. Teller, D. Aurbach, U. Heider and L. Heider, *J. Electrochem. Soc.*, 1999, **146**, 1279-1289.
50. H. Xia, L. Lu and G. Ceder, *J. Power Sources*, 2006, **159**, 1422–1427.
51. S.B. Tang, M.O. Lai and L. Lu, *J. Alloys Comp.*, 2008, **449**, 300–303.
52. Y.-I. Jang, B.J. Neudecker and N.J. Dudney, *Electrochem. Solid-State Lett.*, 2001, **4**, A74-A77.
53. H. Heli, H. Yadegari and A. Jabbari, *J. Appl. Electrochem.*, 2012, **42**, 279–289.
54. K. Dokko, M. Mohamedi, Y. Fujita, T. Itoh, M. Nishizawa, M. Umeda and I. Uchida, *J. Electrochem. Soc.*, 2001, **148**, A422-A426.
55. J. Barker, R. Pynenburg, R. Koksbang and M.Y. Saidi, *Electrochim. Acta*, 1996, **41**, 2481-2488.
56. Y. Zhang, Z.G. Lu, C.Y. Chung and M. Zhu, *Phys. Scr.*, 2007, **T129**, 38–42.
57. K. Nakamura, H. Ohno, K. Okamura, Y. Michihiro, T. Moriga, I. Nakabayashi and T. Kanashiro, *Solid State Ionics*, 2006, **177**, 821–826.
58. J.N. Reimers and J.R. Dahn, *J. Electrochem. Soc.*, 1992, **139**, 2091-2097.
59. T. Ohzuku and A. Ueda, *J. Electrochem. Soc.*, 1994, **141**, 2972-2977.
60. A. Van der Ven, G. Ceder, M. Asta and P.D. Tepesch, *Phys. Rev. B*, 2001, **64**, 184307.
61. K. Kang and G. Ceder, *Phys. Rev. B*, 2006, **74**, 094105.
62. G. Nuspl, M. Nagaoka, K. Yoshizawa, F. Mohri and T. Yamabe, *Bull. Chem. Soc. Jpn.*, 1998, **71**, 2259-2265.
63. S.E. Boulfelfel, G. Seifert and S. Leoni, *J. Mater. Chem.*, 2011, **21**, 16365-16372.
64. J. Yang and J.S. Tse, *J. Phys. Chem. A*, 2011, **115**, 13045–13049.
65. P. Van Rysselberghe, *J. Phys. Chem.*, 1932, **36**, 1152-1155.